Article

Effect of UV Irradiation on the Structural Variation of Metal Oxide-Silica Nanocomposites for Enhanced Removal of Erythromycin at Neutral pH

Yasaman Ghaffari [1,2] , Soyoung Beak [2], Jiyeol Bae [1,2], Md Saifuddin [3] and Kwang Soo Kim [1,2,*]

[1] Department of Environmental Research, University of Science and Technology (UST), Daejeon 34113, Korea; yasaman@kict.re.kr (Y.G.); baejiyeol@kict.re.kr (J.B.)
[2] Department of Environmental Research, Korea Institute of Civil Engineering and Building Technology (KICT), Goyang 10223, Korea; soyoung@kict.re.kr
[3] Department of Environment Engineering, Inha University, Incheon 22212, Korea; md.saifuddin2012@vitalum.ac.in
[*] Correspondence: kskim@kict.re.kr

Abstract: In this study, the effect of UV treatment on the physicochemical properties and structural variation of metal oxide-silica nanocomposites (Mn_2O_3-Fe_2O_3@SiO_2) has been investigated. Based on the results, UV irradiation significantly affects the nanocomposite structure, where SiO_2 network reconfiguration, change in surface OH group density, and surface area were observed. Erythromycin (ERY) has been chosen as a module pollutant to compare the performance of the pristine and UV-treated nanocomposites. The pristine nanocomposite had a high adsorption efficiency (99.47%) and photocatalytic activity (99.57%) at neutral pH for ERY in the first cycle, and this efficiency decreased significantly for the multiple cycles. However, different results have been observed for the UV-treated nanocomposite, where it retained its performance for ten consecutive cycles. This enhanced performance is attributed to the structural modifications after UV exposure, where increased surface area, pore volume, and OH group density resulted in an increased number of the possible mechanisms responsible for the adsorption/oxidation of ERY. Moreover, oxidation of adsorbed molecules by UV light after each cycle can also be another reason for enhanced removal. For the first time, the fate of ERY is studied using regenerated nanocomposites after the last cycle. LC/MS/MS results showed that ERY degraded in 20 min, and the produced reaction by-products were adsorbed by nanocomposites. This study could be a foundation research for the practical approaches for the regeneration of nanomaterials and the successful removal of organic pollutants from aquatic environments.

Keywords: UV-assisted regeneration; porous nanocomposites; pharmaceutical degradation; environmental remediation

1. Introduction

In recent decades, dyes, phenols, heavy metals, antibiotics, pesticides, and polycyclic aromatic hydrocarbons are among the most important pollutants that require special management [1]. Antibiotics have been extensively used a considerable amount in medicine and veterinary fields for various purposes [2]. Usually, antibiotics cannot completely metabolize in the body and are excreted via urine and feces and transported to the wastewater treatment plants. Since the conventional treatment processes are not adequate to remove the emerging micropollutants, they eventually enter the aquatic environment and find their way to the groundwater, drinking water, and soil [3]. Residual antibiotics in the aquatic environment can cause toxicity to the organisms and induce the occurrence of antibiotic resistance genes (ARGs) and antibiotic resistance bacteria (ARB), which have become a severe problem worldwide [4]. According to Decision 495/2015 by the European Union,

the macrolide antibiotics, including azithromycin, clarithromycin, and erythromycin, are named in the "watchlist" substances that should be monitored in the aquatic environment [5]. Erythromycin (ERY) and its corresponding ARGs, including ereA, ermA, ermB, mefA, and mphB, are repeatedly reported in the wastewater effluent streams and rivers in many countries [6]. Many studies reported toxic levels of ERY in various organisms and animals [7]. Marine photosynthetic organisms, especially cyanobacteria, are vital in nutrient cycles and the lives of other organisms in the ocean, and they can be affected even at µg/L concentrations of erythromycin, damaging their growth and metabolism. It has been reported that 60 µg L^{-1} of erythromycin could significantly hinder the physiological process, including primary photochemistry, electron transportation, photophosphorylation, and carbon assimilation in *Selenastrum capricornutum* [8]. Furthermore, severe liver tissue damage was reported in Crucian Carp fish in the study performed by Liu et al. [9]. Therefore, it is necessary to develop a practical approach to decrease ERY in the aquatic environment.

Heterogeneous photocatalysis (HP) is an effective process to overcome the antibiotics problem. However, most of the time, the reaction occurs in acidic pH, requiring pre- and post-treatment of the solution [10]. Bue et al. investigated removal rates of carbamazepine, diclofenac, ibuprofen, ketoprofen, and clofibric acid using mesoporous silica SBA-15. The results showed that high removal efficiency for individual pharmaceuticals was achieved in acidic media (pH 3–5) [11]. Roblero et al. studied the removal of ketoprofen, naproxen, and cimetidine by heterogeneous catalytic ozonation over volcanic sand, and the results showed enhanced removal at pH 4 [12]. Ayoub et al. reported pH 5.5 as the optimum condition for efficiently removing 21 micropollutants (endocrine disruptors, pharmaceuticals, personal care products, and perfluorinated compounds) using an iron-impregnated zeolite catalyst [13].

Adsorption is also efficient for removing micropollutants. However, even the most effective adsorbents, such as activated carbon or MOFs (metal-organic frameworks), cannot solve the problem entirely since most adsorbents are not reusable, and the regeneration techniques are complex and expensive. Chauhan et al. studied the feasibility of Al-pillared clay (Al-PILC) for removing amoxicillin and imipramine, and the results revealed that the adsorption decreased to 50% of its initial adsorption capacity after a second cycle [14]. Prasetya et al. explored the potential of using zirconium-based MOF, called MOF-808, for diclofenac removal, and reported that MOF-808 could withstand at least four adsorption–regeneration cycles [15]. GuilaineJaria et al. used granular activated carbon for the removal of carbamazepine (CBZ), sulfamethoxazole (SMX), and paroxetine (PAR), and utilized it for two cycles [16].

Considering the above drawbacks, developing a sustainable technique for the removal of organic pollutants is highly required. In this study, the impact of UV on the physicochemical properties of Mn_2O_3-$Fe_2O_3@SiO_2$ has been investigated by various characterization techniques, such as X-ray powder diffraction (XRD), Fourier-transform infrared spectroscopy (FTIR), Brunauer–Emmett–Teller (BET) analysis, X-ray photoelectron spectroscopy (XPS), and electron spin resonance (ESR) spectroscopy. The nanocomposite was used to remove erythromycin from aquatic solutions for multiple cycles to determine whether the UV treatment method is suitable for the regeneration of the nanocomposite. Moreover, to the best of our knowledge, there is no study about reaction by-products using regenerated nanocomposites. Hence, LC/MS/MS analysis was performed to study the fate of erythromycin using regenerated nanocomposites after the tenth cycle. We believe that this study can provide the basic knowledge for the future development of sustainable materials for the removal of pharmaceuticals from the contaminated aquatic environment.

2. Results and Discussion

2.1. Texture and Morphology of the Pristine Nanocomposite

In order to evaluate the successful formation of the desired nanocomposite, the texture and morphology of the pristine nanocomposite were analyzed by field emission

scanning electron microscopy (FE-SEM) and high-resolution transmission electron microscope (HR-TEM). FE-SEM was analyzed using Hitachi S-4300, Japan, where the dried nanocomposites were coated with a gold-platinum alloy by ion-sputtering (E-1048 Hitachi ion sputter). The FE-SEM image of the nanocomposite showed a highly porous surface with quasi spheroid morphology (Figure 1a). The HR-TEM images were taken with a field emission TEM (FE-TEM, JEM-2010F, JEOL, Tokyo, Japan). The two-dimensional (2D) elemental mapping was performed by energy-dispersive X-ray spectroscopy (EDX) (X-Maxn 80 T, Oxford, UK). The presence of the metal oxide particles in the silica matrices was confirmed in the HR-TEM image shown in Figure 1b. The Figure 1b inset shows that the crystallite planes were assigned by estimating the fringe width values on the HR-TEM image and then relating it with the inter-planer spacing values from the XRD. The lattice spacing of 0.26 nm matched with Bragg reflection from (104) and (222) planes of Fe_2O_3 and Mn_2O_3, respectively. The results showed that the MOS nanocomposite consists of uniformly distributed Si, Mn, Fe, and O (Figure 1c–g). The 2D mapping of Fe overlapped with the Mn, which indicates the vicinity of Mn_2O_3 and Fe_2O_3 nanoparticles. The EDX data displayed peaks in only the desired atoms, which reveals the absence of impurities during the synthesis and preparation of the nanocomposite. It should be noted that the presence of oxygen in high density can be attributed to adsorbed oxygen. The selected area electron diffraction (SAED) pattern is shown in Figure 1h. Since the silica structure is amorphous, the observed diffraction spots/rings corresponded to metal oxides, which are in accordance with XRD analysis.
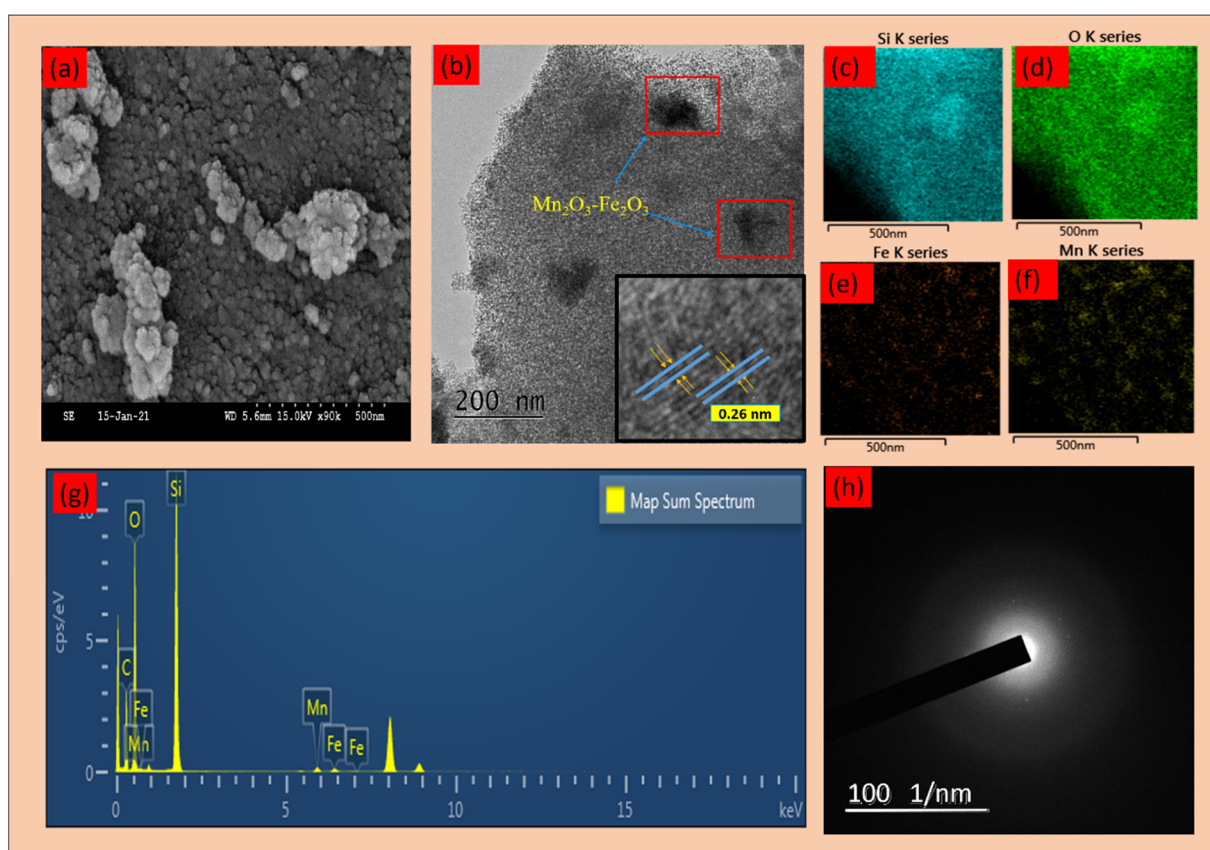

Figure 1. (**a**) FE-SEM image, (**b**) HR-TEM image (inset), (**c**–**f**) 2D mapping of elements, (**g**) elemental spectrum, (**h**) SAED pattern of pristine MOS nanocomposite.

2.2. Performance of Pristine and UV-Treated Nanocomposites for Removal of ERY

The pristine and UV-treated nanocomposites were tested for their ability to remove ERY under adsorption and heterogeneous photo-Fenton processes. Figure 2a shows that

in the first cycle the pristine nanocomposite exhibited excellent removal performance, about 99.58%, and 99.47% for degradation and adsorption respectively. However, this performance decreased for the last cycles and reached 25.12% for adsorption. On the other hand, the efficiency was 82.24% for the last cycle in the degradation process. The kinetic model for degradation has been discussed in Supplementary Figure S1a. Removal of ERY using UV and UV/H_2O_2 as blank experiments also has been shown in Supplementary Figure S1b.
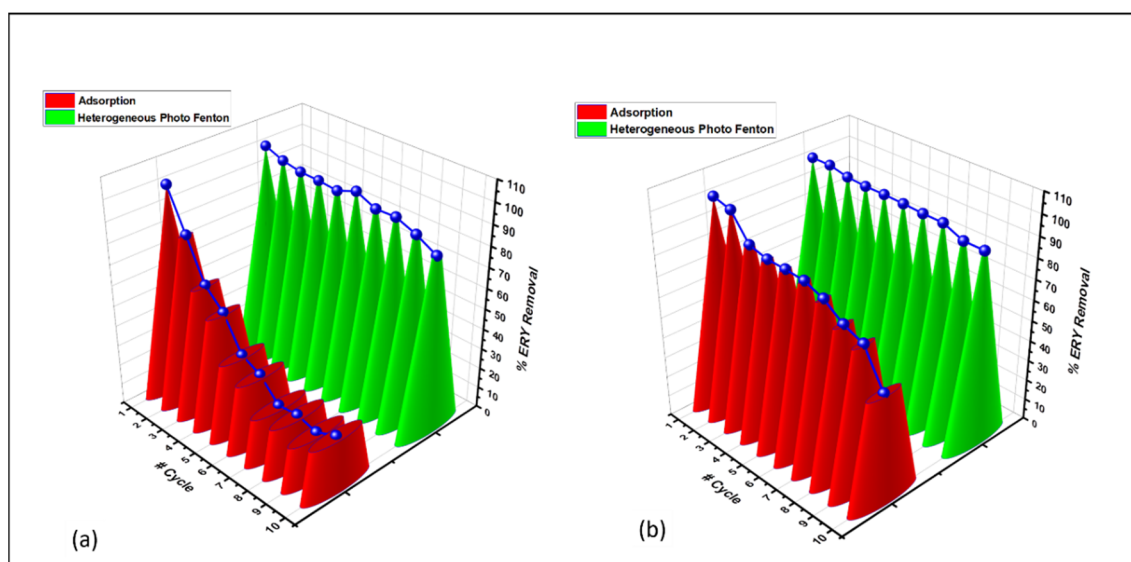

Figure 2. Removal of erythromycin using (**a**) pristine and (**b**) UV-irradiated MOS.

Possible mechanisms for adsorption: Antibiotics' adsorption onto the nanocomposite surface depends on their electrostatic nature and plays an important role, especially in the low initial concentrations. For ERY, different charge forms of ERY can be expected when pH is higher or lower than the pKa (i.e., 8.8.). Similarly, the charge on the nanocomposite surface differs when pH is greater or less than that of the potential of zero charges of the nanocomposite. Hence, the surface charge of the nanocomposite and also the structure of the ERY should be studied. The zeta potential of the nanocomposite has been shown in Supplementary Figure S1. The zero-point charge is the pH when the surface charge of the nanocomposite is zero. The pH drift method was utilized to determine the pHzpc value in this study. The pHzpc was 6.00 for MOS; therefore, MOS has a positive charge if the pH is <6, while the surface is negatively charged if the pH is >6. Since the pH of the solution is 7.3, the nanocomposite surface is negatively charged. The chemical structure of the ERY is shown in Supplementary Figure S1. ERY includes the erythronolide portion, which contains 14 membered lactone rings and 2 sugar-containing polyhydroxylactones. D-desosamine amino sugar is attached to the C-5 portion of the lactone ring. The other sugar, called L cladinose, is attached to the C-3 portion of the lactone ring firmly through a b-glycosidic bond. The protonation/deprotonation of the ERY is based on their pKa values, which control the adsorption of the ERY on the nanocomposite surface due to electrostatic forces. For pH below the pKa values, ERY contains positively charged groups in its structures, while at higher pH values, it is neutral [17]. Thus, at pH 7.3, ERY has a positive charge. On the other hand, according to the zeta potential results, the nanocomposite's surface has a negative charge in this pH. Considering the above, an electrostatic attraction will occur, which will result in better dispersion of the ERY on the nanocomposite surface, improving its adsorption. Moreover, the high specific surface can also improve its adsorption capability. Another possible reason for the high adsorption of ERY on MOS can be the formation of a hydrogen bond between the hydroxyl groups of Si with the oxygens of ERY molecules [18].

Proposed mechanisms for degradation: The hydroxyl radical ($^\bullet$OH) generated from H_2O_2, surface-bound $^\bullet$OH ($^\bullet$OH $_{surf}$), hole (h^+), and the electron (e^-) superoxide ($^\bullet$O$_2^-$) can be considered as reactive species responsible for ERY degradation. Detailed experiments for the main reactive species have been discussed in the Supplementary Figure S2 [1,17,19].

Regeneration/reusability: Erythromycin removal, including adsorption and degradation, was performed for 10 consecutive cycles, in which after every cycle, the catalyst was washed with DI water, dried in the oven (100 °C), and irradiated with UV-C for 20 min. The regeneration and the reusability experiments were conducted under the same conditions mentioned in Section 3.3, except for the catalyst dosage, which was used at 1 g L^{-1} to consider the mass loss during the process. The degradation trend indicated enhanced performance and stability of the nanocomposite under the heterogeneous photo-Fenton reaction, which maintained the performance until the last cycle and showed 91.76% removal even after 10 cycles of operation. For the adsorption process, the efficiency of each cycle was also significantly enhanced compared to the pristine nanocomposite. However, it decreased to 51.18% in the last cycle, probably due to some deposition occurring on the nanocomposite surface (Figure 2b). Table 1 shows the removal efficacy of ERY in this work and in the literature.

Table 1. Comparison of removal efficiency of erythromycin using different nanocomposites.

	Process	Experimental Condition	Removal Efficiency	Reusability/ Regeneration	Ref.
ERY	TiO$_2$/carbon	Catalyst dosage: 1 g/L, initial concentration: 10 mg dm^{-3}, pH: not mentioned	87%	1	[20]
ERY	ZnO/Fe$_3$O$_4$	Catalyst dosage: 50–800 mg/L, initial concentration: 10–100 µg/L, pH: 5	36%	8	[18]
ERY	Znpc–TiO$_2$	Catalyst dosage: 0.4 g/L, initial concentration: 1 × 105 M, pH: 5	74.21%	5	[21]
azithromycin (ERY derivative)	GO@Fe$_3$O$_4$/ ZnO/SnO$_2$	Catalyst dosage: 1 g/L, initial concentration: 30 mg/L, pH: 3	90.06%	6	[22]
ERY	Mn$_2$O$_3$- Fe$_2$O$_3$@SiO$_2$	Catalyst dosage: 0.5 g/L, initial concentration: 2 mg/L, pH: neutral	99.57	10	This work

2.3. Comparison of Structural Variation in Pristine and UV-Treated Nanocomposite

XRD: The change in the nanocomposite structure after the UV irradiation (20 and 180 min) was investigated by XRD (Figure 3). The diffraction patterns were obtained using the Ultima IV (Rigajku, Tokyo, Japan) X-ray diffractometer (XRD) with Cu Kα and a Ni filter, and the scanning speed was set to 3° min^{-1}. The XRD patterns showed a broad diffraction peak at 22.34°, attributed to the amorphous SiO$_2$ network [23]. Only some peaks were designated to Fe$_2$O$_3$ and Mn$_2$O$_3$ crystals due to the low content of Fe and Mn. However, the diffraction peak at 2θ of 32.96° is attributed to α-Mn$_2$O$_3$ (the most intense 222 Bragg reflection) (JCPDS No. 24-508). Two distinct diffraction peaks were observed at 2θ, of 32.96° and 35.30° (the most intense Bragg reflection in 104 and 110), which are attributed to the α-Fe$_2$O$_3$ (JCPDS No. 33-0664) [24]. There was an insignificant change in the XRD spectrum of the MOS after UV exposure, with a slight shift of the peaks towards higher 2θ values. Moreover, the intensity of diffraction peaks slightly increased after UV irradiation. However, the UV exposure did not induce crystal modification or any new crystal formation since no new peaks were observed in the XRD patterns after UV irradiation. Similar results have been reported in a study conducted by Wang et al., where the intensity of diffraction peaks in polyethylene (HDPE)/titanium dioxide (TiO$_2$) composites increased after UV irradiation [25]. The crystallite size (D) of nanocomposites was calculated using the Debye–Scherer formula (D = (kλ/βcos θ)), where k is the shape factor (0.9), λ is the X-ray wavelength (0.15418 nm, CuK$_\alpha$), β is the full width at half maximum (FWHM), and θ is the diffraction angle [26]. The average diameter of the

crystallite size was about 21 nm for the pristine sample, which showed a slight increase and became 23 nm for UV-irradiated samples. This change can be due to the slight increase in the intensity of diffraction peaks after UV irradiation. The lattice parameters for α-Fe$_2$O$_3$ were *a* (5.00 Å) and *c* (13.6 Å), and for α-Mn$_2$O$_3$ was 9.2 Å, which have not been changed, suggesting that UV light does not affect the lattice parameters.
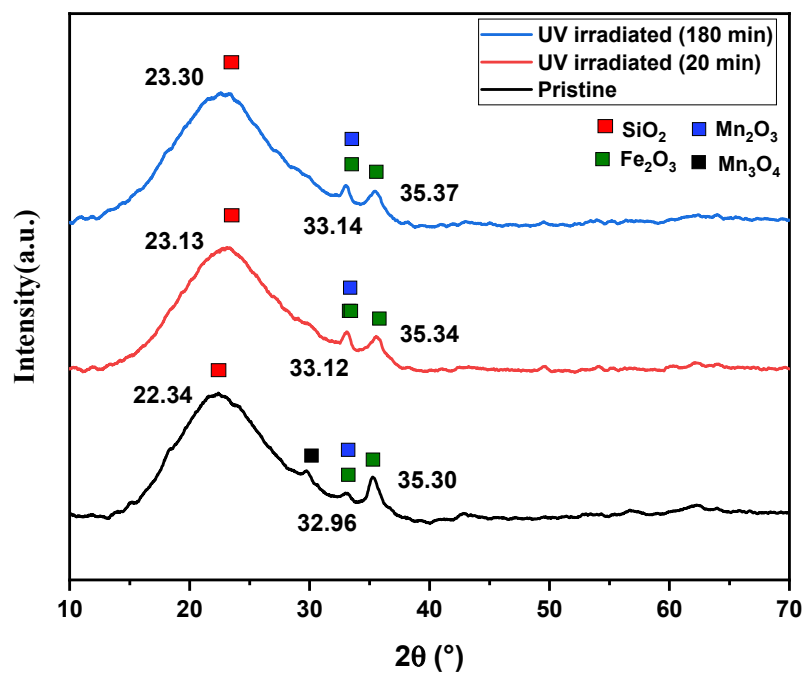

Figure 3. XRD patterns of pristine and UV-irradiated MOS nanocomposites.

FTIR: In order to obtain a better understanding of the structure and composition of the pristine and UV-irradiated samples, the Fourier-transform infrared (FTIR) analysis was carried out in the range of 400–4000 cm^{-1} (Figure 4). FTIR spectra of samples were recorded using KBr pellets over a FTIR spectrometer (Cary670, USA, California, Agilent). The recording was performed with a single-beam spectrometer with 60 added scans. All of the samples showed peaks at the same location with various intensities. The absorption band is related to antisymmetric stretching of Si-O-Si (1088 cm^{-1}), and the symmetric mode of Si-O-Si (810 cm^{-1}), stretching vibration of Si-OH (945 cm^{-1}), and bending of Si-O (457 cm^{-1}) were observed, which implies the SiO$_2$ network [27]. It should be noted that the peak at 945 cm^{-1} was weakened because the Si–O–Si bond and SiO$_2$ network were formed by dewatering of the silanol group in the calcination process [19]. In the FTIR spectrum of nanocomposites, the band at 3446 cm^{-1} is due to the surface hydroxyl groups, and the low-intensity band at 1628 cm^{-1} is attributed to the O–H bending mode of the adsorbed water molecules [28]. Stretching vibration of the M–O bond (metal oxides) in the MO$_6$ octahedron and MO$_4$ tetrahedron indicates the presence of the Si-O bond with metals, which is hidden here due to overlapping with the Si-O band at 457 cm^{-1}. A low-intensity peak at 1711 cm^{-1} was ascribed to the carboxylic group stretching vibration of C=O due to the fuels used in this work [19]. A significant change has been observed in the FTIR spectra of UV-irradiated samples in all the peaks (Figure 4a). The increased intensity at ~945 cm^{-1} (corresponding to Si-OH) is due to the formation of new hydroxyl groups, which was confirmed by the increased intensity of the 3435 cm^{-1} band shown in Figure 4b. The strained Si–O–Si bonds may have shattered and rearranged as a SiO$_2$ network with higher content of OH groups, which can be one of the reasons for enhanced performance of the nanocomposite, especially in the adsorption process since it can increase the number of the hydrogen bonds between the hydroxyl groups of Si with the oxygens of ERY molecules.

It should be noted that this finally brings more ERY molecules in the vicinity of the MOS and increases the chance of degradation along with adsorption.
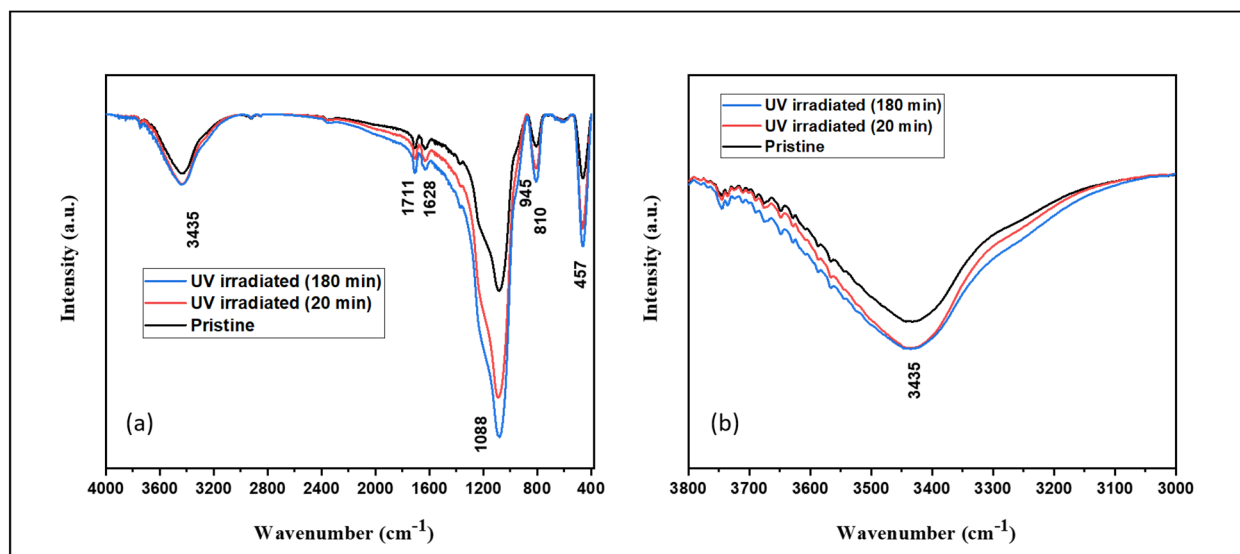

Figure 4. (**a**) FTIR spectra (4000–400 cm^{-1}), (**b**) FTIR spectra (3800–3000 cm^{-1}) of pristine and UV-irradiated MOS.

BET: Porosity properties and specific surface area of pristine and UV-irradiated nanocomposites were analyzed by the N$_2$ adsorption–desorption isotherm (Figure 5). For Brunauer–Emmett–Teller (BET) analysis, the N$_2$ adsorption–desorption isotherm was measured at 77 K in a Gemini series Micromeritics 2360 instrument. Before subjecting the nanocomposites for BET analysis, samples were degassed at 473 K for 2 h with a Micromeritics FlowPrep 060. As shown in Figure 5, the sorption isotherm of all nanocomposites was type IV with an H2(b) hysteresis loop in the relative pressure range of 0.45–0.9, which belongs to the structure of mesoporous materials [29]. Based on the Brunauer–Emmett–Teller method, pristine MOS has a specific surface area (S_{BET}) of 891.58 m^2/g, which increased to 1025.19 and 1038.67 for 20 and 180 min of UV irradiation.
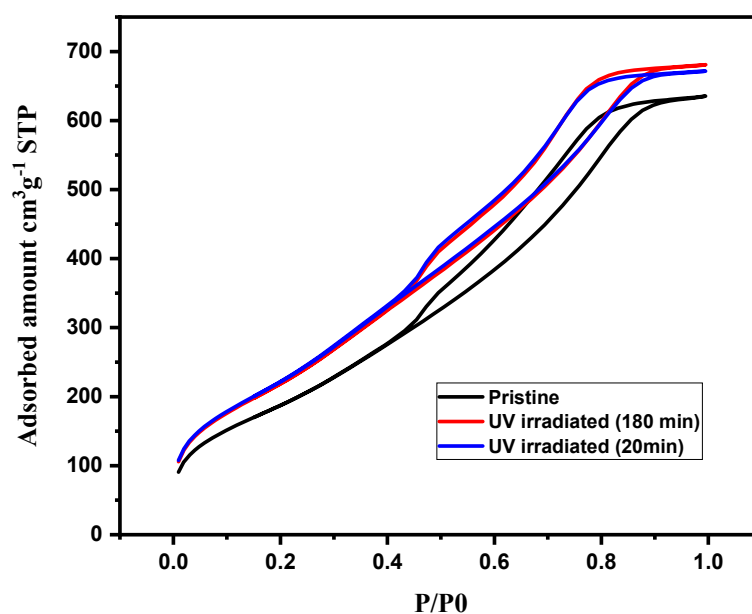

Figure 5. N$_2$ adsorption-desorption curve of pristine and UV-irradiated MOS.

Parameters such as S_{BET}, pore volume, and average pore diameter have been listed in Table 2. Total pore volume has also slightly increased from 0.98 to 1.039 and 1.059. However, the pore diameter decreased after subjecting the pristine nanocomposite to UV irradiation. In the present case, the reconfiguration of the SiO_2 network occurred in a non-uniform way, leading to a decreased pore diameter and increased surface properties. Since the surface area was high and increased even more after UV exposure, it resulted in successive adsorption–degradation cycles. Another reason for the enhanced performance in the adsorption of ERY is that an increase in pore volume increases the chances of ERY diffusion, which directly favors the adsorption. This diffusion can also affect the degradation process by better scattering the ERY on the active sites that exist on the surface, which finally results in better degradation. Moreover, oxidation of residual organic molecules on the surface and pores of the nanocomposite can also be considered as another reason for the regeneration ability of the UV-treated MOS.

Table 2. Porosity and surface area of pristine and UV-irradiated nanocomposites.

	Product	BET (m^2/g)	Pore Volume (cm^3/g)	Pore Diameter (nm)
1	Pristine	891.58	0.982	5.4
2	UV-irradiated (20 min)	1025.190	1.039	4.9
3	UV-irradiated (180 min)	1038.67	1.053	4.8

HRXPS: For the elemental oxidation state and surface chemical composition before and after UV exposure, nanocomposites were examined using X-ray photoelectron spectroscopy (XPS) analysis. A K-alpha XPS instrument (Thermo Scientific Inc., East Grinstead, England, UK) with a monochromatic Al Kα X-ray source was utilized, and the pressure was chosen to be 4.8×10^{-9} mbar. High-energy resolution scans of the Si 2p, Mn 2p, Fe 2p, and O 1s, of pristine and UV-irradiated nanocomposites and associated components, are shown in Figure 6a–l. It should be noted that the concentration of Fe and Mn was low, which resulted in the absence of peaks in the full spectra in Figure 6a–c. As depicted in Figure 6d, the HRXPS O 1s spectrum for the pristine nanocomposite has been deconvoluted using Gaussian distribution functions. The HRXPS O 1s spectrum revealed peaks at 531.45, 532.50, 533.48, and 534.68 eV, corresponding to M–O (M: metal), Si–O–Si, O–H, and physisorbed water molecules, respectively [30].

The fraction of Si–O bonds decreased by 30~35% for the UV-irradiated samples after 20 and 180 min of UV exposure, respectively. The area under the O–H peak increased by 60~64% after irradiation (Figure 6e,f), and the increase in the OH density in the FTIR spectrum supports this fact. These results strongly suggested that the SiO_2 network was affected by UV photons and resulted in structural modifications. The decreased area for the Si–O curve implies that part of the Si–O–Si bonds could be broken and generate new Si-OH groups. As mentioned in the FTIR analysis, the generation of the new hydroxyl groups can be involved in the enhanced performance of nanocomposites in removing ERY. It should be noted that enhanced performance after increasing the number of OH groups indicates that surface-bound •OH (•OH$_{surf}$) was one of the main reactive species responsible for the degradation process.

The Fe 2p spectrum of the pristine sample has been shown in Figure 6g, and the two peaks centered at 710.53 eV for Fe 2p$_{3/2}$ and 724.55 eV for Fe 2p$_{1/2}$ show that Fe exists in the form of Fe^{3+} [31]. The HRXPS Fe 2p spectrum of MOS after 20 and 180 min of UV irradiation showed a shift of 0.89 and 1.25 eV in the binding energy of Fe 2p$_{1/2}$, respectively (Figure 6h,i). The HRXPS Fe 2p spectrum of MOS after 20 and 180 min of UV irradiation showed a shift of 0.2 and 0.3 Fe 2p$_{3/2}$. These changes are not considered very significant in the Fe environment, and Fe stayed as Fe^{3+}. The Figure 6j spectrum shows the spin-orbital doublets centered at 641.15 eV for Mn 2p$_{3/2}$ and 652.72 eV for Mn 2p$_{1/2}$, which imply Mn^{3+} [32]. The HRXPS Mn 2p spectrum of MOS after 20 and 180 min

of UV irradiation showed a shift of 0.35 and 0.48 eV in the binding energy of Mn $2p_{3/2}$, respectively (Figure 6h,i). The HRXPS Mn 2p spectrum of MOS after 20 and 180 min of UV irradiation showed a shift of 0.49 and 0.64 Mn $2p_{1/2}$, which shows an insignificant change in metal species. Fe and Mn stayed in the form of Fe^{3+} and Mn^3, and no isolated metal formed after UV exposure.
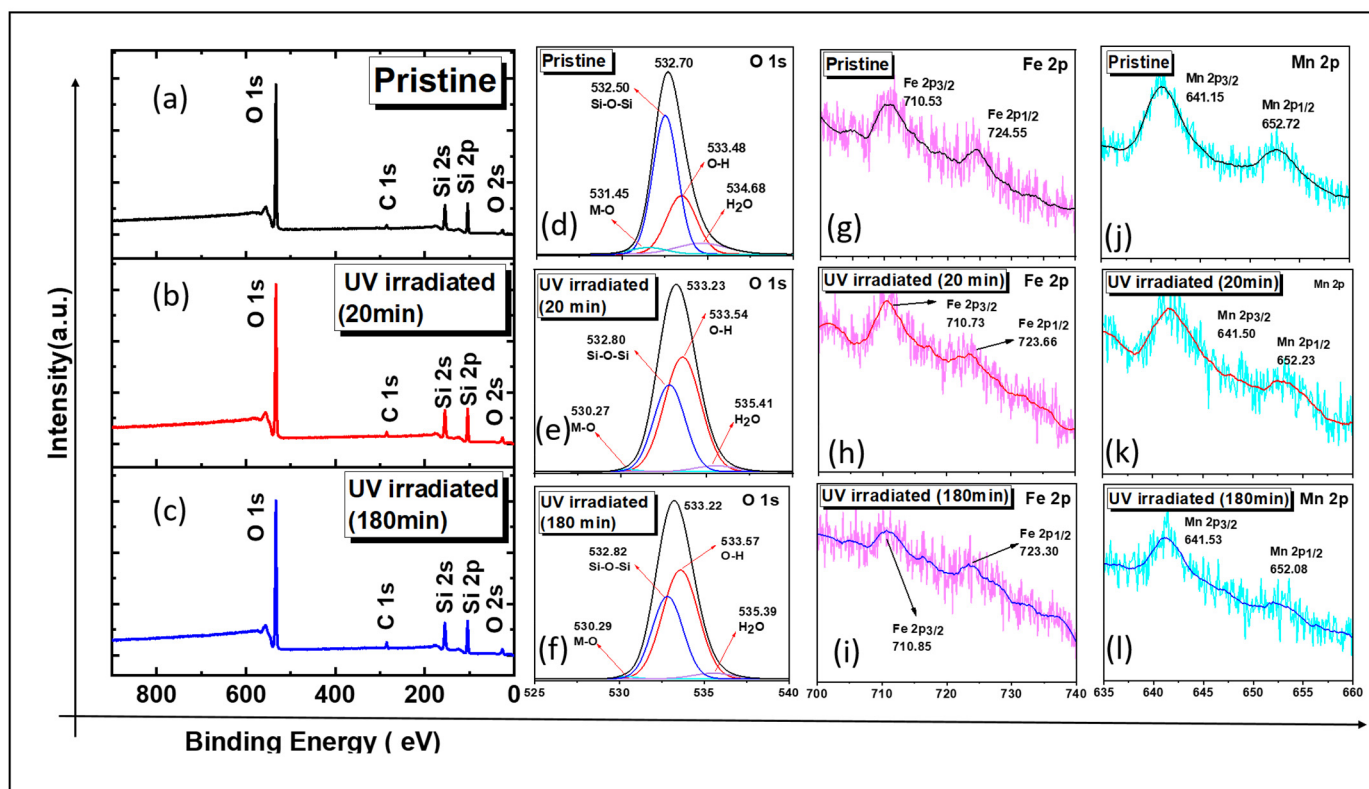

Figure 6. (**a–c**) HRXPS full spectrum of nanocomposites, (**d–f**) HRXPS O 1s spectra, (**g–i**) HRXPS Fe 2p spectra, (**j–l**) HRXPS Mn 2p spectra of pristine and UV-irradiated MOS.

ESR: The ESR spectra have been used to detect different oxidation states, metal complexes, and chemical environments of atoms. The ESR spectra at room temperature before and after UV irradiation are shown in Figure 7a–c. It can be seen that the ESR spectra showed a single broad signal in all of the nanocomposites, and no new signal was observed. The g value of 2.02–2.03 shows the combined contribution of Fe as Fe_xO_y clusters or Fe_2O_3 nanoparticles in the silica matrix [33]. It should be noted that isolated Fe^{3+} shows the signal at 4.30, and the absence of this signal is proof that isolated Fe^{3+} did not form after UV exposure. For the Mn, no ESR signal was found in any of the samples since Mn^{3+} is ESR-silent, and it did not change for UV-irradiated samples, suggesting that Mn remained in the same state. It should be noted that other forms of manganese have an intense sextet which is not found here, further proving that Mn stayed in the form of Mn^{3+}. These findings support our findings by XPS.
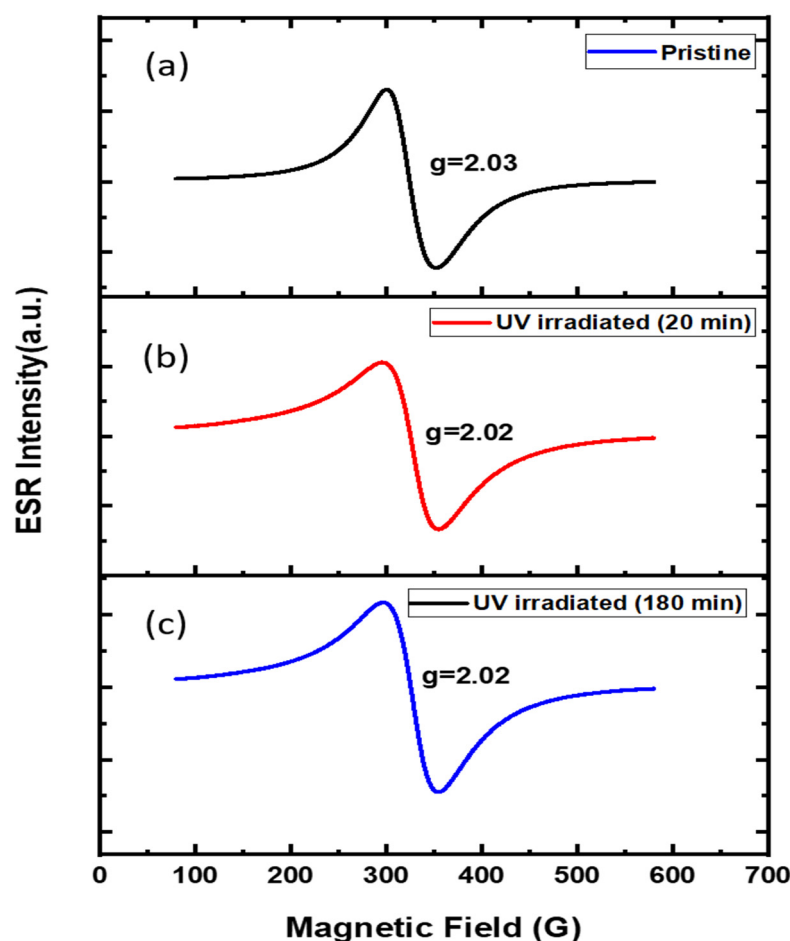
Figure 7. ESR spectra of (**a**) pristine, (**b**) UV-irradiated (20 min), and (**c**) UV-irradiated (180 min) MOS.

2.4. Degradation By-Products Using the Regenerated Nanocomposite after the Last Cycle

The reaction by-products using pristine nanomaterials have been studied in past decades. However, to the best of our knowledge, there is no study using regenerated nanocomposites after the last cycle. To further study the quality of regenerated nanocomposites after the last cycle, by-products of the heterogeneous photo-Fenton reaction after 20 and 120 min have been studied using LC/MS/MS, and the detailed methodology is shown in Supplementary Table S1. The results imply that after a 20 min irradiation time, ERY was significantly decomposed. This is evident by the decrease in the ERY peak intensity and the observation of new peaks corresponding to ERY photocatalytic products. Figure 8 shows a full-scan mass spectrum initial ERY, infused at 0.5 mL min^{-1} using a syringe pump. The identification of transformation products focused on the most abundant compounds formed during the first 20 min of the reaction, according to their molecular masses, retention times, and empirical formulas. The MS spectra of the parent ERY reside on its molecular masses [MH]$^{+}$, ERY (734.4681) [18]. In this work, the two most abundant intermediate s(m/z: 421 and m/z: 290) were observed after 20 min of reaction. However, after 120 min, these peaks disappeared, due to the successful adsorption of by-products by the highly porous nanocomposite used in this study.
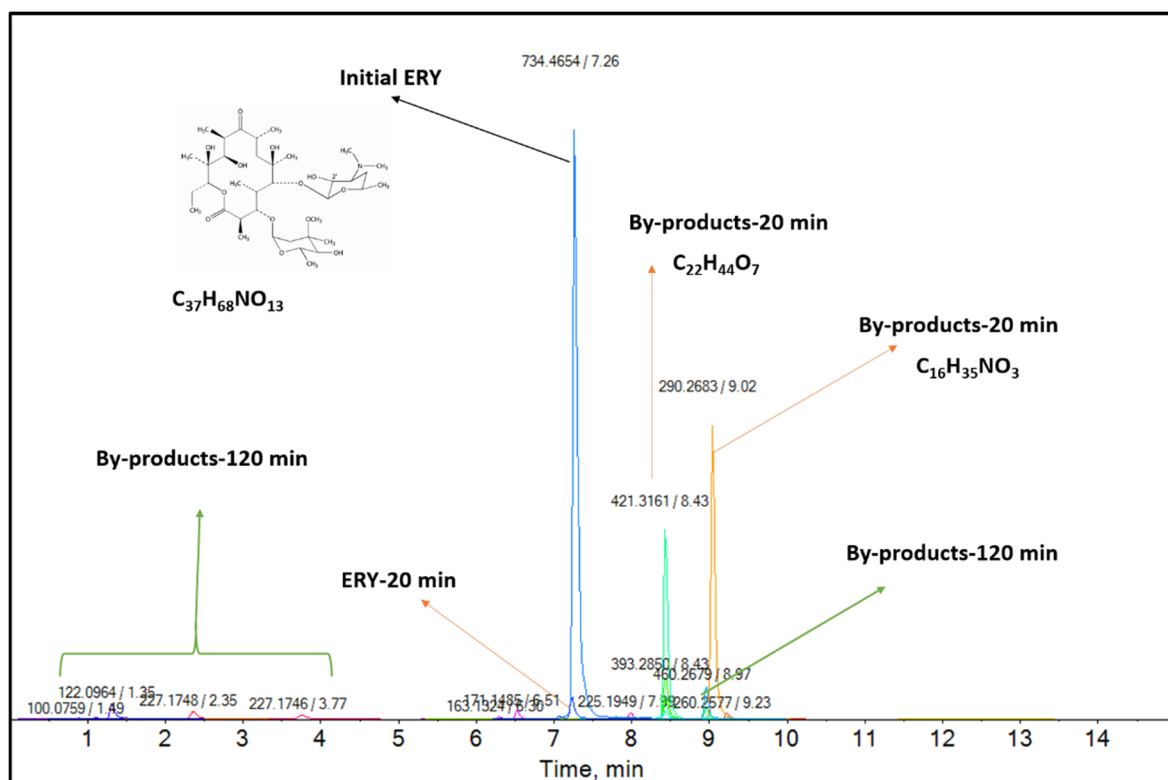
Figure 8. ERY degradation by-products using regenerated nanocomposites after the last cycle.

3. Materials and Methods

3.1. Chemicals and Reagents

Manganese(II) nitrate tetrahydrate ($Mn(NO_3)_2 \cdot 4H_2O$) (>98%), cetyltrimethylammonium chloride (CTAC) solution (25 wt.%), and erythromycin were supplied by Sigma Aldrich, Germany. Ferric(III) nitrate nonahydrate ($Fe(NO_3)_3 \cdot 9H_2O$), urea, and tetraethyl orthosilicate 95% (TEOS) were purchased from Samchun Pure Chemicals, Seoul, Korea. Sodium hydroxide (1N NaOH) and hydrogen peroxide (28% H_2O_2) solutions were procured from Daejung Chemicals and Metals Co., Ltd., Siheung, Korea. All the chemicals were used without any further purification. The UV lamps used were purchased from Philips, Amsterdam, The Netherlands.

3.2. Synthesis of Metal Oxide Silica Nanocomposites

The Mn_2O_3-Fe_2O_3@SiO_2 nanocomposites were prepared according to our previously published procedure with slight modifications [19]. In summary, Mn_2O_3-Fe_2O_3@SiO_2 nanocomposites were synthesized using the sol-gel/combustion method. In a typical synthesis, 1 g of $Mn(NO_3)_2 \cdot 4H_2O$ and 1.16 g of $Fe(NO_3)_3 \cdot 9H_2O$ were added to 60 mL of cetyltrimethylammonium chloride (25% H_2O) and mixed for 30 min at 40 °C. Then, 2 g of urea (fuel) was added to the solution and mixed for another 30 min. In the next step, 40 mL of TEOS was added dropwise to the solution. The solution was incubated at 60 °C for 24 h. Then, the sample was calcined at 550 °C for 6 h. The obtained metal oxide silica was coded as MOS.

3.3. Experimental Procedure

Erythromycin (ERY) was used as a module pollutant to examine the performance of pristine and regenerated nanocomposites under heterogeneous photo-Fenton and adsorption processes. For this purpose, 200 mL of ERY solution (2 mg L^{-1}) was poured into a quartz glass, and then 25 mmol L^{-1} of 28% H_2O_2 was added to the solution. Then, 100 mg of the nanocomposite was added to the previous solution. No pH adjustments were made,

and the pH of the solution was 7.3. Finally, the mixture was irradiated with UV light. The experiments were conducted using a black acrylic reactor with a quartz tube in the middle and four UV lamps parallel to the quartz tube. During the experiments, the reactor temperature was maintained at 25 °C using cooling fans connected to the bottom of the reactor. The UV-C lamp (8 W, λmax = 254 nm, Philips) was used as the irradiation source. Samples were collected at specific time intervals and filtered to eliminate the particles. Adsorption experiments were conducted under the same conditions without light and H_2O_2.

Detection and analysis: Erythromycin concentration was analyzed by LC/MS/MS, Thermo Vanquish (Thermo Scientific, Waltham, MA, USA), and the column used was Waters Cortects C18 (2.1 × 100, 1.6 μm). The detailed analysis methodology has been tabulated in Supplementary Materials Table S1.

4. Conclusions

In this study, the effect of UV treatment on the structural variations and regeneration of Mn_2O_3-Fe_2O_3@SiO_2 was studied by experimental and spectroscopic analysis. It was evident that there was a significant change in the silica network, hydroxyl groups, and porosity properties of the nanocomposite after UV exposure. The pristine nanocomposite showed an excellent ERY adsorption/degradation performance. The high adsorption efficiency was due to electrostatic attraction, high surface area, and the possibility of hydrogen bonding. The high degradation efficiency was due to the high surface area and reactive species produced in the degradation reaction. However, the pristine nanocomposite could not retain its performance for ten cycles. On the other hand, the UV-irradiated nanocomposite showed enhanced removal efficiency for ten consecutive cycles. FTIR and XPS analysis showed that silica network reconfiguration after UV irradiation with an increased hydroxyl density could increase the possible mechanism involved with adsorption/degradation. Enhanced performance after increasing the OH groups could indicate the vital role of surface-bound $^{\bullet}OH$ ($^{\bullet}OH_{surf}$) in the removal process. BET analysis showed that the surface area was high and even increased after UV exposure, resulting in successive adsorption–degradation cycles. Additionally, increased pore volume may have favored the diffusion of ERY molecules.

For this reason, MOS showed an excellent ERY removal performance even after ten cycles. Moreover, these observations can be due to the oxidation of residual organic molecules on the surface or in the pores of the nanocomposite. For the first time, the fate of ERY was studied using regenerated nanocomposites after the last cycle. LC/MS/MS results suggested that the fabricated nanocomposite is not only reusable but can also be a dual functional nanomaterial, which could break down the parent compound and adsorb the formed reaction by-products. This study could be a foundation research for the practical approaches for the regeneration of nanomaterials and the successful removal of organic pollutants from aquatic environments.

Supplementary Materials: The following supporting information can be downloaded at: https://www.mdpi.com/article/10.3390/catal12040424/s1, Figure S1: (a) Degradation kinetic modeling of ERY under UV/H_2O_2/MOS system, (b) Removal of ERY using pristine nanocomposite, (c) Zeta potential of MOS, (d) Chemical structure of ERY; Figure S2: Radical scavenger experiment; Table S1: Detailed methodology for ERY analysis using LC/MS/MS.

Author Contributions: Conceptualization, Methodology, Data curation, Formal analysis, software, Writing the original draft. Y.G.; Investigation, S.B. and M.S.; Resources S.B.; Funding acquisition, Project administration J.B.; Supervision, Visualization, K.S.K. All authors have read and agreed to the published version of the manuscript.

Data Availability Statement: Not applicable.

Conflicts of Interest: The authors declare no conflict of interest.

References

1. Humayun, M.; Wang, C.; Luo, W. Recent Progress in the Synthesis and Applications of Composite Photocatalysts: A Critical Review. *Small Methods* **2022**, *6*, 2101395. [CrossRef] [PubMed]
2. Patel, M.; Kumar, R.; Kishor, K.; Mlsna, T.; Pittman, C.U., Jr.; Mohan, D. Pharmaceuticals of emerging concern in aquatic systems: Chemistry, occurrence, effects, and removal methods. *Chem. Rev.* **2019**, *119*, 3510–3673. [CrossRef]
3. Bao, T.; Damtie, M.M.; Hosseinzadeh, A.; Frost, R.L.; Yu, Z.M.; Jin, J.; Wu, K. Catalytic degradation of P-chlorophenol by muscovite-supported nano zero valent iron composite: Synthesis, characterization, and mechanism studies. *Appl. Clay Sci.* **2020**, *195*, 105735. [CrossRef]
4. Schafhauser, B.H.; Kristofco, L.A.; de Oliveira, C.M.R.; Brooks, B.W. Global review and analysis of erythromycin in the environment: Occurrence, bioaccumulation and antibiotic resistance hazards. *Environ. Pollut.* **2018**, *238*, 440–451. [CrossRef] [PubMed]
5. Michael-Kordatou, I.; Iacovou, M.; Frontistis, Z.; Hapeshi, E.; Dionysiou, D.D.; Fatta-Kassinos, D. Erythromycin oxidation and ERY-resistant Escherichia coli inactivation in urban wastewater by sulfate radical-based oxidation process under UV-C irradiation. *Water Res.* **2015**, *85*, 346–358. [CrossRef]
6. Chu, L.; Zhuan, R.; Chen, D.; Wang, J.; Shen, Y. Degradation of macrolide antibiotic erythromycin and reduction of antimicrobial activity using persulfate activated by gamma radiation in different water matrices. *Chem. Eng. J.* **2019**, *361*, 156–166. [CrossRef]
7. González-Pleiter, M.; Gonzalo, S.; Rodea-Palomares, I.; Leganés, F.; Rosal, R.; Boltes, K.; Marco, E.; Fernández-Piñas, F. Toxicity of five antibiotics and their mixtures towards photosynthetic aquatic organisms: Implications for environmental risk assessment. *Water Res.* **2013**, *47*, 2050–2064. [CrossRef]
8. Liu, B.; Nie, X.; Liu, W.; Snoeijs, P.; Guan, C.; Tsui, M.T.K. Toxic effects of erythromycin, ciprofloxacin and sulfamethoxazole on photosynthetic apparatus in Selenastrum capricornutum. *Ecotoxicol. Environ. Saf.* **2011**, *74*, 1027–1035. [CrossRef]
9. Liu, J.; Lu, G.; Ding, J.; Zhang, Z.; Wang, Y. Tissue distribution, bioconcentration, metabolism, and effects of erythromycin in crucian carp (*Carassius auratus*). *Sci. Total Environ.* **2014**, *490*, 914–920. [CrossRef]
10. Bao, T.; Damtie, M.M.; Wei, W.; Phong Vo, H.N.; Nguyen, K.H.; Hosseinzadeh, A.; Cho, K.; Yu, Z.M.; Jin, J.; Wei, X.L.; et al. Simultaneous adsorption and degradation of bisphenol A on magnetic illite clay composite: Eco-friendly preparation, characterizations, and catalytic mechanism. *J. Clean. Prod.* **2021**, *287*, 125068. [CrossRef]
11. Bui, T.X.; Choi, H. Adsorptive removal of selected pharmaceuticals by mesoporous silica SBA-15. *J. Hazard. Mater.* **2009**, *168*, 602–608. [CrossRef]
12. Sáenz-Roblero, B.; Durán, J.E.; Masís-Mora, M.; Ramírez-Morales, D.; Rodríguez-Rodríguez, C.E. Removal of cimetidine, ketoprofen and naproxen by heterogeneous catalytic ozonation over volcanic sand at low pH. *J. Water Process Eng.* **2020**, *37*, 101461. [CrossRef]
13. Ayoub, H.; Roques-Carmes, T.; Potier, O.; Koubaissy, B.; Pontvianne, S.; Lenouvel, A.; Guignard, C.; Mousset, E.; Poirot, H.; Toufaily, J.; et al. Iron-impregnated zeolite catalyst for efficient removal of micropollutants at very low concentration from Meurthe river. *Environ. Sci. Pollut. Res.* **2018**, *25*, 34950–34967. [CrossRef] [PubMed]
14. Chauhan, M.; Saini, V.K.; Suthar, S. Removal of pharmaceuticals and personal care products (PPCPs) from water by adsorption on aluminum pillared clay. *J. Porous Mater.* **2020**, *27*, 383–393. [CrossRef]
15. Prasetya, N.; Li, K. MOF-808 and its hollow fibre adsorbents for efficient diclofenac removal. *Chem. Eng. J.* **2021**, *417*, 129216. [CrossRef]
16. Jaria, G.; Calisto, V.; Silva, C.P.; Gil, M.V.; Otero, M.; Esteves, V.I. Fixed-bed performance of a waste-derived granular activated carbon for the removal of micropollutants from municipal wastewater. *Sci. Total Environ.* **2019**, *683*, 699–708. [CrossRef]
17. Ashraf, A.; Liu, G.; Yousaf, B.; Arif, M.; Ahmed, R.; Irshad, S.; Cheema, A.I.; Rashid, A.; Gulzaman, H. Recent trends in advanced oxidation process-based degradation of erythromycin: Pollution status, eco-toxicity and degradation mechanism in aquatic ecosystems. *Sci. Total Environ.* **2021**, *772*, 145389. [CrossRef]
18. Fernández, L.; Gamallo, M.; González-Gómez, M.; Vázquez-Vázquez, C.; Rivas, J.; Pintado, M.; Moreira, M. Insight into antibiotics removal: Exploring the photocatalytic performance of a Fe_3O_4/ZnO nanocomposite in a novel magnetic sequential batch reactor. *J. Environ. Manag.* **2019**, *237*, 595–608. [CrossRef] [PubMed]
19. Ghaffari, Y.; Beak, S.; Bae, J.; Kim, S.; Saifuddin, M.; Kim, K.S. One-step fabrication of novel ultra porous $Mn_2O_3-Fe_2O_3@SiO_2$: A versatile material for removal of organic pollutants from industrial wastewater at neutral pH. *Sep. Purif. Technol.* **2022**, *285*, 120259. [CrossRef]
20. Maletić, M.; Vukčević, M.; Kalijadis, A.; Janković-Častvan, I.; Dapčević, A.; Laušević, Z.; Laušević, M. Hydrothermal synthesis of $TiO_2/carbon$ composites and their application for removal of organic pollutants. *Arab. J. Chem.* **2019**, *12*, 4388–4397. [CrossRef]
21. Vignesh, K.; Rajarajan, M.; Suganthi, A. Photocatalytic degradation of erythromycin under visible light by zinc phthalocyanine-modified titania nanoparticles. *Mater. Sci. Semicond. Processing* **2014**, *23*, 98–103. [CrossRef]
22. Sayadi, M.H.; Sobhani, S.; Shekari, H. Photocatalytic degradation of azithromycin using GO@ $Fe_3O_4/ZnO/SnO_2$ nanocomposites. *J. Clean. Prod.* **2019**, *232*, 127–136. [CrossRef]
23. Bogdanchikova, N.; Pestryakov, A.; Farias, M.; Diaz, J.A.; Avalos, M.; Navarrete, J. Formation of TEM-and XRD-undetectable gold clusters accompanying big gold particles on $TiO_2–SiO_2$ supports. *Solid State Sci.* **2008**, *10*, 908–914. [CrossRef]
24. Chen, G.; Nengzi, L.-C.; Gao, Y.; Zhu, G.; Gou, J.; Cheng, X. Degradation of tartrazine by peroxymonosulfate through magnetic Fe_2O_3/Mn_2O_3 composites activation. *Chin. Chem. Lett.* **2020**, *31*, 2730–2736. [CrossRef]

25. Wang, S.; Zhang, J.; Liu, L.; Yang, F.; Zhang, Y. Evaluation of cooling property of high density polyethylene (HDPE)/titanium dioxide (TiO$_2$) composites after accelerated ultraviolet (UV) irradiation. *Sol. Energy Mater. Sol. Cells* **2015**, *143*, 120–127. [CrossRef]

26. Nasseh, N.; Panahi, A.H.; Esmati, M.; Daglioglu, N.; Asadi, A.; Rajati, H.; Khodadoost, F. Enhanced photocatalytic degradation of tetracycline from aqueous solution by a novel magnetically separable FeNi$_3$/SiO$_2$/ZnO nano-composite under simulated sunlight: Efficiency, stability, and kinetic studies. *J. Mol. Liq.* **2020**, *301*, 112434. [CrossRef]

27. Motlagh, M.M.; Hassanzadeh-Tabrizi, S.; Saffar-Teluri, A. Influence of Mn$_2$O$_3$ content on the textural and catalytic properties of Mn$_2$O$_3$/Al$_2$O$_3$/SiO$_2$ nanocatalyst. *Ceram. Int.* **2014**, *40*, 16177–16181. [CrossRef]

28. Alizadeh, A.; Fakhari, M.; Safaei, Z.; Khodeai, M.; Repo, E.; Asadi, A. Ionic liquid-decorated Fe$_3$O$_4$@ SiO$_2$ nanocomposite coated on talc sheets: An efficient adsorbent for methylene blue in aqueous solution. *Inorg. Chem. Commun.* **2020**, *121*, 108204. [CrossRef]

29. Naik, S.P.; Elangovan, S.; Okubo, T.; Sokolov, I. Morphology control of mesoporous silica particles. *J. Phys. Chem. C* **2007**, *111*, 11168–11173. [CrossRef]

30. Reddy, B.M.; Khan, A.; Yamada, Y.; Kobayashi, T.; Loridant, S.; Volta, J.-C. Surface characterization of CeO$_2$/SiO$_2$ and V$_2$O$_5$/CeO$_2$/SiO$_2$ catalysts by Raman, XPS, and other techniques. *J. Phys. Chem. B* **2002**, *106*, 10964–10972. [CrossRef]

31. Flak, D.; Chen, Q.; Mun, B.S.; Liu, Z.; Rękas, M.; Braun, A. In situ ambient pressure XPS observation of surface chemistry and electronic structure of α-Fe$_2$O$_3$ and γ-Fe$_2$O$_3$ nanoparticles. *Appl. Surf. Sci.* **2018**, *455*, 1019–1028. [CrossRef]

32. Yang, Z.; Zhang, W.; Wang, Q.; Song, X.; Qian, Y. Synthesis of porous and hollow microspheres of nanocrystalline Mn$_2$O$_3$. *Chem. Phys. Lett.* **2006**, *418*, 46–49. [CrossRef]

33. Mimouni, I.; Bouziani, A.; Naciri, Y.; Boujnah, M.; El Belghiti, M.A.; El Azzouzi, M. Effect of heat treatment on the photocatalytic activity of α-Fe$_2$O$_3$ nanoparticles: Towards diclofenac elimination. *Environ. Sci. Pollut. Res.* **2021**, *29*, 7984–7996. [CrossRef] [PubMed]